

A numerical study of tornadogenesis in a rotating thunderstorm

By R. K. SMITH

and

L. M. LESLIE

*Department of Mathematics, Monash University,
Clayton, Australia, 3168*

*Australian Numerical Meteorology Research Centre,
P.O. Box 5089AA, Melbourne, Australia, 3001*

(Received 24 February 1978; revised 18 July 1978)

SUMMARY

The structure and dynamics of tornadoes and the mechanisms leading to their formation are explored in the context of an axis-symmetric numerical model of a tornado cyclone. The paper extends a recent study of tornadogenesis by the authors to include explicit representation of moisture effects.

The calculations show that the distribution of buoyancy in the updraught of a severe 'supercell' thunderstorm can account for the generation and maintenance of an intense tornado when the level of rotation in the storm is within the observed range of values. The simulated vortex extends to high levels in the cloud but maximum swirling velocities occur within the lowest kilometre or two above the ground in concordance with recent Doppler radar observations.

For a fixed vertical distribution of ambient temperature and moisture, the vortex strength is sensitive to the imposed circulation: if the latter is too small, the cloud updraught rotates weakly but there is no evidence of a vortex or a funnel cloud; if it is too strong, a vortex and its associated funnel cloud may form but terminate aloft. This explains why only a few apparently suitable thunderstorms spawn damaging tornadoes.

The effects of surface friction on vortex strength and structure are studied in some detail and the results suggest that the terminating inflow layer at the ground may have a less important control on the vortex dynamics than has hitherto been supposed.

1. INTRODUCTION

Tornadoes are narrow vortices with violently rotating winds which extend to the ground beneath intense cumulonimbus clouds, or occasionally beneath rapidly developing congestus clouds on the flanks of severe thunderstorms. Locally they are the most ferocious and destructive wind storms in nature. A reduction in pressure in the vortex leads to condensation of subcloud moisture so that it takes on the characteristic appearance of a pendant funnel cloud protruding through the parent cloud base and terminating at the ground. A large fraction of embryonic tornadoes fail to develop to ground level but exhibit suspended funnels which terminate aloft – these are known as 'funnel clouds'.

Fortunately, tornadoes are comparatively rare, being produced by less than one per cent of thunderstorms. They are also small in horizontal extent, with diameters normally between twenty-five and five hundred metres, and the majority are short lived, being on the ground for no more than a few minutes. For these reasons, however, and because of their extreme violence, they have been difficult to study observationally and their origin and dynamics have remained an enigma in meteorological science. A succinct review is given by Davies-Jones and Kessler (1974).

Conventional meteorological instruments seldom survive the passage of a tornado overhead and the rudimentary knowledge of wind fields acquired so far is based largely on patterns and severity of damage, together with photogrammetric analyses of the motion of cloud wisps in the funnel cloud and of debris caught up in the lower parts of the vortex. Nothing was known about the vortex above cloud base until recently, when a detailed observational study of the 1973 Union City tornado led to the exciting discovery of a 'tornadic vortex signature'* (TVS) during Doppler radar surveillance of the storm (Burgess *et al.* 1975a, b; Brown *et al.* 1978). This radar 'signature', which is believed to indicate the

* In early papers following its discovery, the signature was described as a 'gate-to-gate shear', or GGS.

presence of concentrated vortical motion, was first observed at mid-levels within the storm 23 minutes before the tornado touched the ground. During this period the TVS extended progressively to lower levels, reaching cloud base simultaneously with funnel cloud appearance. After touchdown the tornado and the TVS moved together and the signature disappeared rapidly with the demise of the vortex. Whilst the tornado was on the ground, radar scans at different elevations revealed vertical continuity of the TVS up to an altitude of ten kilometres, evidence that the tornado had considerable vertical extent. More recent cases in which tornadoes or funnel clouds have been clearly associated with vortex signatures are reported by Brown and Lemon (1976).

Larger tornadoes, comprising perhaps one to five per cent of reported tornadoes, are generally the most severe and long lived and they account for almost all tornado injuries and fatalities and most of the damage. They may exist for up to an hour or two and create damage paths many hundreds of metres wide and up to two hundred kilometres long, with maximum winds in the range 75 to 110 m s^{-1} (about 270–400 kph). These tornadoes are usually associated with massive rotating thunderstorms, alternatively called 'tornado cyclones' or 'mesocyclones', which are of the supercell type (Browning 1965; Marwitz 1972), having a single intense updraught often penetrating several kilometres into the stratosphere. Supercell storms have a degree of organization which enables them to propagate undiminished in strength for many hours and, besides producing occasional severe tornadoes, they may also produce copious amounts of large hail. In this paper, we shall focus our attention on tornadoes spawned from such storms.

Observations of wind fields in mesocyclones using Doppler radar techniques reveal the existence of ample circulation about the updraught through sufficient depths to account for the observed circulation of a severe tornado (Burgess 1976; Brandes 1977a, b). Accordingly, there seems little reason to doubt that the tornado acquires its high rate of rotation by a further concentration of this mesoscale source and it is equally likely that the concentration is caused by the strong buoyant acceleration in the storm updraught. Indeed, we shall subsequently show in detail how this concentration can be accomplished. It is difficult to conceive another mechanism capable of maintaining the huge pressure reduction across the vortex core, which for intense vortices has been estimated to be in excess of 100 mb. The possibility that thunderstorm electricity could play a significant role in driving the flow has been rejected by Davies-Jones and Golden (1975), and although there have been numerous suggestions that a vigorous downdraught might initiate and even sustain the vortex (e.g. Rossmann 1960; Danielsen 1975; Eskridge and Das 1976; but see Smith *et al.* 1977), these have not in our view been convincingly demonstrated by complete and self-consistent dynamical models, either in the laboratory or numerically. It also seems unlikely that any buoyancy in the core produced by latent heat release in the funnel cloud plays a dominant role in driving the vortex, otherwise one might expect to see some tornadoes without a parent cloud, or to see them forming prior to their parent cloud (Morton 1966, p. 163). Davies-Jones (private communication) points out that this possibility can also be ruled out on energy budget considerations.

To explore the dynamics of a vortex driven from aloft in the presence of ambient rotation, we recently carried out some experiments with a simple numerical model which simulates these features (Smith and Leslie 1978; Leslie and Smith 1978; henceforth referred to as TG and LS respectively). In the model, the updraught of the tornado cyclone is represented by an axial body force located in the central upper portion of a cylindrical region of air and rotation is imposed by specifying the swirling velocity of air which enters through the radial boundary of the region. The calculations show in detail how a vortex is generated aloft when the body force is applied and how it develops downwards. They also confirm the important prediction of Morton (1969, p. 325) that concentrated vortex

formation requires the forcing strength and the level of rotation to be confined within a narrow range of values. This explains why relatively few storms spawn vortices. We have also shown that downward vortex growth is impeded if the imposed rotation is confined to middle or upper levels within the cloud and/or if the subcloud air is stably stratified. In each case we have demonstrated the possibility of generating steady vortices which terminate aloft, analogous to funnel clouds.

For an imposed circulation typical of a tornado cyclone and with the body force strength chosen within the parameter range for which a concentrated vortex will form, the vortices described in TG and LS are realistic in size and strength *vis-à-vis* severe tornadoes. In addition, when the thickness of the computational region is large enough to encompass a substantial depth of cloud (say 8 km or more), our vortex growth times are comparable with those observed for the downward development of tornadic vortex signatures from cloud mid-levels to the ground. However, for the spatial distribution of body force used in these experiments, it is not possible to determine an appropriate body force strength on the basis of cloud buoyancy data (TG, p. 196) and the crucial question remains as to whether the buoyancy field within a severe storm updraught is capable of producing an intense tornado as we have speculated. An affirmative answer to this question is obtained herein using an extended version of the model in LS; the principal modification being the inclusion of moisture effects, and hence latent heat release. Our present study also explores in detail the dynamics of vortices driven by buoyancy within an organized cloud updraught.

2. FORMULATION OF THE MODEL

(a) Basic equations

The flow domain over which computations are performed is a cylindrical region of air of radius R and depth H , with its axis vertical. The lower boundary is at the ground but air may enter or leave the region in a normal direction through the side and upper boundaries. The flow is taken to be axi-symmetric and rotation is imposed by prescribing a swirling velocity component on air entering through the side boundary.

The equations we use are a more general version of the approximate set derived by Ogura and Phillips (1962) for studies of deep convection in a nearly adiabatic atmosphere. The principal approximation here is the neglect of radial and temporal variations of density in the continuity equation, whereas the momentum equations are unapproximated except for the usual diffusion terms representing turbulent shear stresses. Thus the continuity, momentum and thermodynamic equations can be written in the form:

$$\partial(r\rho_a u)/\partial r + \partial(r\rho_a w)/\partial z = 0 \quad . \quad . \quad . \quad (1)$$

$$Du/Dt - v^2/r = -c_p\theta \partial\Pi'/\partial r + K_M(\nabla^2 u - u/r^2) \quad . \quad . \quad (2)$$

$$Dv/Dt + uv/r = K_M(\nabla^2 v - v/r^2) \quad . \quad . \quad . \quad (3)$$

$$Dw/Dt = -c_p\theta \partial\Pi'/\partial z + g\theta'/\theta_a + K_M\nabla^2 w \quad . \quad . \quad (4)$$

$$\text{and} \quad D\theta/Dt = \dot{h}/(c_p\Pi) + K_H\nabla^2\theta \quad . \quad . \quad . \quad (5)$$

using the nomenclature:

r, ϕ, z	a cylindrical coordinate system coaxial with the flow and with its origin at the ground
u, v, w	corresponding velocity components
t	time

In this simple formulation, the rate of latent heat release is given by

$$\dot{h} = \begin{cases} 0, & \text{if } q_w < q_{vs} \\ -L Dq_{vs}/Dt, & \text{if } q_w > q_{vs} \end{cases} \quad (8)$$

Finally, q_{vs} is evaluated using the formula

$$q_{vs} = 6.11\varepsilon/(p_{00}\Pi^{1/\kappa}) \cdot \exp\{(L/R_v)(1/273 - T^{-1})\} \quad (9)$$

where ε ($=0.62$) is the ratio of molecular weights of water vapour and dry air, R_v ($\approx 461 \text{ J kg}^{-1} \text{ K}^{-1}$) is the specific gas constant for water vapour, L ($= 2.5 \times 10^6 \text{ J kg}^{-1}$) is the latent heat of evaporation for water and p_{00} is expressed in millibars (see, e.g., Hess 1959, pp. 49 and 55).

(c) Boundary conditions

The complete set of boundary conditions on u , v , w , θ , Π' and q_w are illustrated in Fig. 1. The conditions on velocity and potential temperature at the axis ensure smooth radial gradients of w and θ , appropriate for a flow with diffusion, and axial symmetry. At the radial boundary, air is constrained to enter horizontally with a prescribed tangential velocity component V_e and with ambient potential temperature $\theta_a(z)$. Moreover, since $w = 0$, continuity implies that $\partial(\rho_a r u)/\partial r = 0$ at this boundary.

$$u = 0, \quad \frac{\partial v}{\partial z} = 0, \quad \frac{\partial}{\partial z}(\rho_a w) = 0, \quad \frac{\partial \theta}{\partial z} = \begin{cases} -\frac{L}{c_p \Pi} \frac{\partial q_{vs}}{\partial z} & , \text{ if } q_w > q_{vs} \\ 0 & , \text{ if } q_w < q_{vs} \end{cases}$$

$$\frac{\partial \Pi'}{\partial z} = \frac{1}{c_p \theta} \left[K_M \nabla^2 w + \frac{g \theta'}{\theta_a} - \frac{\partial w}{\partial t} \right]$$

$$\begin{aligned} u &= 0 \\ v &= 0 \\ \frac{\partial w}{\partial r} &= 0 \\ \frac{\partial \theta}{\partial r} &= 0 \\ \frac{\partial \Pi'}{\partial r} &= \frac{K_M}{c_p \theta} \frac{1}{r} \frac{\partial}{\partial r} \left(r \frac{\partial u}{\partial r} \right) \end{aligned}$$

$$\frac{\partial \Pi'}{\partial r} = \frac{1}{c_p \theta} \left[K_M \left(\nabla^2 u - \frac{u}{R^2} \right) + \frac{V_e^2}{R} - \frac{\partial u}{\partial t} - u \frac{\partial u}{\partial r} \right]$$

$$q_w = q_a(z)$$

$$\left(\frac{\partial u}{\partial z}, \frac{\partial v}{\partial z} \right) = C_D (u^2 + v^2)^{\frac{1}{2}} (u, v), \quad w = 0$$

$$\begin{aligned} r = 0 \quad \theta &= \theta_a(0), \quad \frac{\partial \Pi'}{\partial z} = \frac{K_M}{c_p \theta} \frac{\partial^2 w}{\partial z^2} \quad r = R \end{aligned}$$

Figure 1. Schematic representation of the flow domain together with the boundary conditions used in the calculations.

At the lower boundary there is no normal flow but the tangential flow satisfies the condition

$$(\partial u / \partial z, \partial v / \partial z) = C_D(u^2 + v^2)^{1/2}(u, v) \quad (10)$$

which corresponds with no slip when the constant C_D is infinite, partial slip when it is finite, and free slip (or no stress) when it is zero. The potential temperature is held fixed at the ground, equal to its ambient value there. For a stably stratified atmosphere ($\partial\theta/\partial z > 0$), this results in a flux of heat to the ground, but as we choose parameters in the regime where the flow is controlled by advective rather than diffusive processes (see section 2(e)) this flux has little dynamical significance and the condition $\partial\theta/\partial z = 0$ would serve equally well (Smith *et al.* 1975).

At the upper boundary, the radial velocity and the vertical gradients of azimuthal and vertical velocity are taken to be zero. These are especially mild constraints when the vortex becomes established and are consistent at zero order with the 'boundary layer' nature of 'long-thin' vortices as deduced from scaling analyses (Morton 1966, 1969). It is also assumed that the sensible heat flux through this boundary is due to advection only: where clear air ($q_w < q_{vs}$) leaves the region, this requires the vertical gradient of potential temperature to be zero, but in the cloudy air ($q_w > q_{vs}$) condensation continues with height and the vertical gradient of equivalent potential temperature must vanish,* i.e. $\partial\theta/\partial z = -(L/c_p\Pi)\partial q_{vs}/\partial z$.

The boundary conditions on Π' are obtained using either Eq. (2) or (4), together with the conditions on velocity and potential temperature. These constitute a set of Neumann-type conditions for Π' , which satisfies an elliptic equation in the computational region. Hence, for a unique determination of Π' , we assume that the perturbation pressure along the perimeter of the computational region at ground level is zero and that the total pressure is equal to its ambient value of 1000 mb. Then $\Pi'(R, \phi, 0) = 0$ and $\Pi(R, \phi, 0) = \Pi_a(0) = 1$ for $0 < \phi < 2\pi$, enabling $\Pi_a(z)$ to be determined uniquely from the prescribed distribution of $\theta_a(z)$.

Finally, since the water conservation equation (7) is purely advective, it is necessary to specify q_w only at points on the boundary where air enters the computational region, in this case along the radial boundary. Accordingly we take $q_w(R, z, t) = q_a(z)$ for $0 \leq z \leq H$.

(d) Initial conditions

Prior to the initial instant $t = 0$, the air is at rest, with the moisture and potential temperature distributions equal to their respective ambient values, $q_a(z)$ and $\theta_a(z)$, chosen as typical of a conditionally unstable atmosphere. At $t = 0$, a uniform potential temperature excess of 2 K is imposed over a cylindrical region in the height range from $\frac{1}{3}H$ to $\frac{2}{3}H$ and with radius $\frac{1}{3}R$. The associated buoyancy perturbation initiates motions which release the conditional instability, leading to the rapid formation of an axi-symmetric cloud. As the cloud updraught forms, it simultaneously acquires rotation, and vortex development ensues.

(e) Experiment specifications

A total of six numerical experiments are studied: one is regarded as the prototype and the others are variants of this, each in one respect only. The size of the computational region is larger than that used in TG and LS, with $R = 3$ km and $H = 8$ km. Also, $g =$

* For saturated air, the equivalent potential temperature is defined by $\theta_e = \theta \exp(Lq_{vs}/c_p T)$; thus $\partial\theta_e/\partial z = [\partial\theta/\partial z + (\theta L/c_p T) \partial q_{vs}/\partial z - (\theta L q_{vs}/c_p T^2)] \exp(Lq_{vs}/c_p T)$ and the third term in parenthesis is ordinarily negligible compared with the first two: see, e.g., Hess 1959, p. 55.

9.8 m s^{-2} , $c_p = 1005 \text{ J kg}^{-1} \text{ K}^{-1}$, and in the prototype experiment, $V_e = 2.0 \text{ m s}^{-1}$, corresponding to a circulation, $\Gamma = 2\pi R V_e$, equal to $3.8 \times 10^4 \text{ m}^2 \text{ s}^{-1}$ and a mean vertical vorticity, $\Gamma/\pi R^2$, equal to $1.3 \times 10^{-3} \text{ s}^{-1}$ – typical of a tornado cyclone, and $K_M = K_H = 2.5 \text{ m}^2 \text{ s}^{-1}$, corresponding to a ‘pseudo-Reynolds-number’, Γ/K_M , equal to 1.5×10^4 and a ‘pseudo-Prandtl-number’, K_M/K_H , equal to unity. Unless otherwise stated, the no-slip condition $u = 0$, $v = 0$, is taken at the lower boundary, and, in all the experiments, the ambient thermal and moisture distributions are specified by

$$\theta_a(z) = (295.5 + 4.5z) \text{ K} \quad (11)$$

and
$$q_a(z) = \begin{cases} (14.0 - 2.8z) \text{ g kg}^{-1}, & 0 \leq z \leq 5 \text{ km} \\ 0 \text{ g kg}^{-1}, & z > 5 \text{ km} \end{cases} \quad (12)$$

when z is expressed in kilometres. Figure 4 displays these distributions in an aerological diagram.

The six equations are further defined in Table 1.

TABLE 1. THE NUMERICAL EXPERIMENTS AND THEIR DEVIATION FROM THE PROTOTYPE EXPERIMENT, NUMBER TWO

Experiment	Variation from the prototype
1	A non-rotating cloud, $V_e = 0 \text{ m s}^{-1}$
2	
3	$V_e = 2.5 \text{ m s}^{-1}$
4	$V_e = 3.0 \text{ m s}^{-1}$
5	Partial slip at ground, $C_D = 1$
6	Free slip at ground, $C_D = 0$

(f) The numerical method

The equations of motion are integrated in primitive form using the method described by Williams (1969). Briefly, the prognostic equations (2)–(4) and (7) are written in the form $\partial\eta/\partial t = \text{a function of } u, v, w, \theta, q_w, \Pi'$ and their space derivatives, where η is one of the dependent variables u, v, w, q_w . This set of equations may be integrated in time, using centred time and space differences in the same manner as Williams. The remaining equations are implicit in θ and Π' owing to the dependence of q_{vs} on temperature, i.e. on Π and θ . Thus, using Eqs. (6), (8) and (9), the prognostic equation for θ has the form

$$\partial\theta/\partial t = \text{a function of } u, w, \theta, \Pi' \text{ and their space derivatives, and of } \partial\Pi'/\partial t \quad (13)$$

and Π' is determined by an elliptic equation with the form

$$\partial\{r\rho_a\partial\Pi'/\partial r\}/\partial r + \partial\{r\rho_a\partial\Pi'/\partial z\}/\partial z = \text{a function of } u, v, w, \theta \text{ and their space derivatives} \quad (14)$$

obtained by taking $\partial(r\rho_a \times \text{Eq. (2)})/\partial r + \partial(r\rho_a \times \text{Eq. (4)})/\partial z$ and using continuity (Eq. (1)) to eliminate the time derivative. The former equation can be used to update θ only if $\partial\Pi'/\partial t$ is known, whereas the latter requires the updated value of θ before it can be solved for the new distribution of Π' . This implicitness was recognized by Ogura and Phillips (1962) and studied further by Wilhelmson and Ogura (1972). The last named authors have performed calculations which show that in the case of a cumulus cloud, the effect of the pressure perturbation on the calculation of saturated mixing ratio for water vapour is an order of magnitude smaller than a scale analysis would suggest and that it may be neglected. Since

the radial pressure variation across a tornado is considerably higher than in a cloud, we have used the local value of pressure to calculate q_{vs} but have ignored the term $\partial \Pi' / \partial t$ in Eq. (13). This is unlikely to result in any serious errors in view of the short timestep used in the calculations (see below) and, of course, the effect diminishes as the steady state is approached. Our method therefore consists of updating the distributions of u, v, w, q_w and θ , followed by a diagnosis of the pressure field. The latter is accomplished by solving Eq. (14) by successive over-relaxation. This cycle is then repeated for each timestep until the desired total number of timesteps is reached. For details of the differencing scheme, the reader is referred to Williams's paper or to Eskridge and Das (1976, pp. 74–75). The method uses a staggered grid (Fig. 2) in which the Exner function, potential temperature, tangential

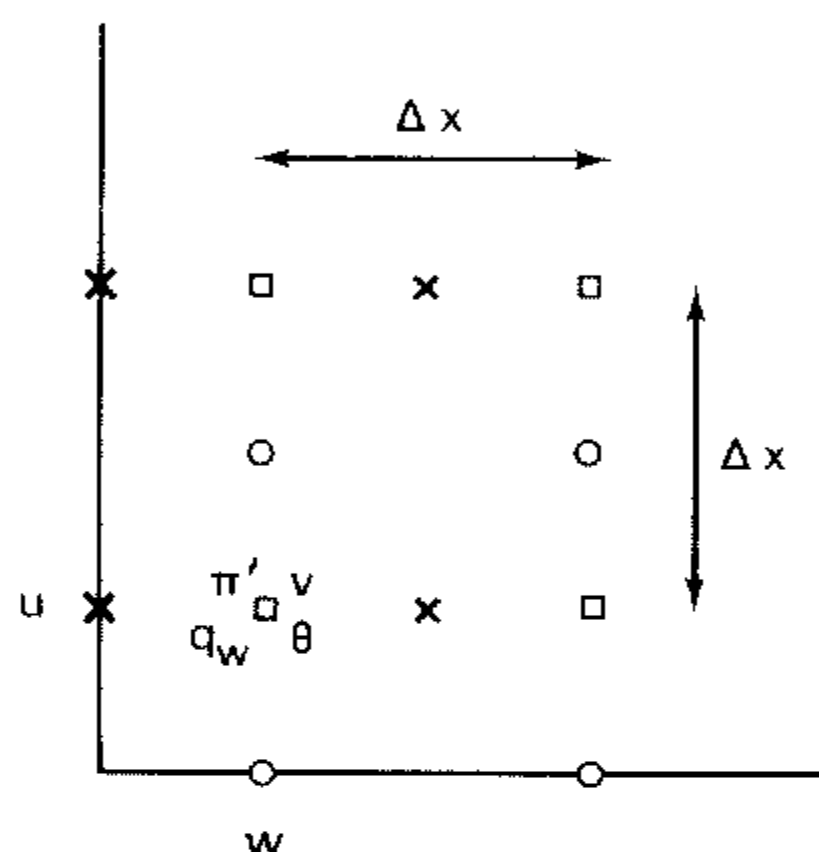


Figure 2. The staggered grid network used in the finite difference approximation to the equations.

velocity and moisture variable are specified at the same points, whereas the u and w velocity components are defined at different points. The grid spacing, Δx , as indicated in Fig. 2 is 25 m.

The timestep employed in most of the calculations was 0.3 s. About 2500 timesteps were required for each steady-state calculation.

3. RESULTS

As in our earlier papers TG and LS, it is useful to tabulate the following data pertaining to the steady state of each numerical experiment:

- w_{\max} – the maximum vertical velocity,
- v_{\max} – the maximum swirling velocity,
- r_{\max} – the radius at which v_{\max} occurs,
- Δp – the maximum pressure reduction across the vortex,
- A – the 'amplification factor', defined as $(v_{\max}/r_{\max})/(V_e/R)$, a measure of the angular rotation of the vortex compared with the ambient field of rotation, and
- T_F – the time taken to reach a steady state, based on the arbitrary criterion that the total kinetic energy changes by less than one percent over ten timesteps. In cases where a vortex develops to the lower boundary, it does so in a time which is approximately $0.85 T_F$.

These quantities are listed in Table 2.

TABLE 2. STEADY-STATE FLOW DATA; SEE TEXT FOR DETAILS

Experiment	r_{\max} (m)	v_{\max} (m s ⁻¹)	w_{\max} (m s ⁻¹)	Δp (mb)	A	T_F (min)
1			20	2.5		12½
2	41	60	63	46	2200	13½
3	48	52	58	33	1300	13½
4	53	45	51	28	850	14
5	39	66	61	52	2540	13½
6	38	70	59	56	2760	13½

(a) *A non-rotating updraught ($V_e = 0$)*

As a preliminary to investigating vortex growth we consider the steady, axi-symmetric cloud in experiment 1, where there is no imposed swirl. The streamlines, isentropes, water vapour mixing ratio isopleths, and the cloud boundary for this flow are shown in Fig. 3. The shape of the cloud is determined by the detailed vertical distributions of temperature and moisture in the environment and is constrained by the assumption of axial symmetry.

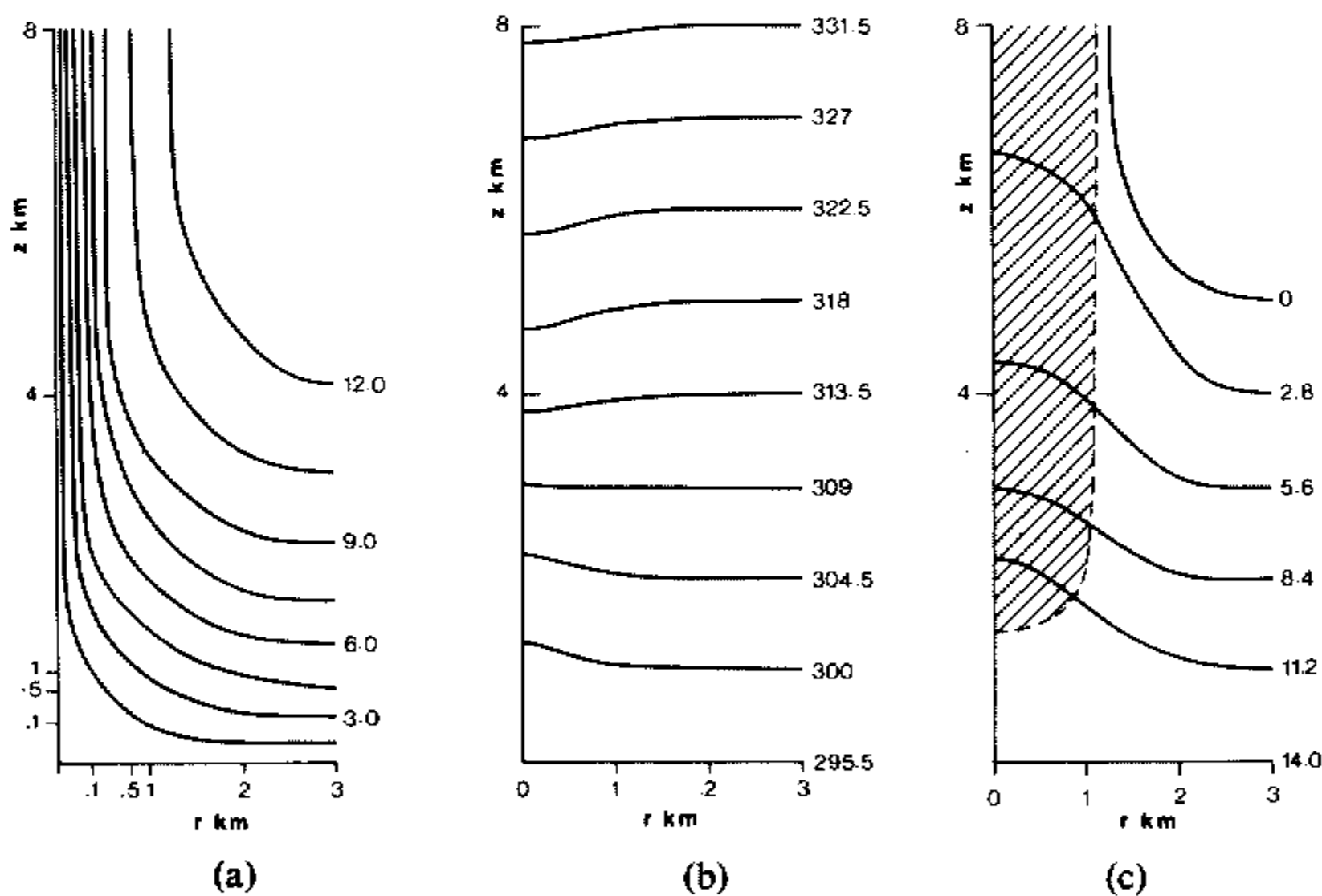


Figure 3. Solutions for the steady-state, axi-symmetric cloud in experiment 1: (a) streamlines, labelled in units of $10^6 \text{ m}^2 \text{ s}^{-1}$, (b) isentropes, labelled in K, (c) water vapour mixing ratio isopleths, labelled in g kg^{-1} , and the cloud (shaded region). In (a), the coordinates have been stretched logarithmically in the L-shaped region $0 < r < 1 \text{ km}$ or $0 < z < 1 \text{ km}$ to overcome the bunching of contours near the axis and near the surface.

In this experiment, the shape bears only broad resemblance to an actual cloud but since the updraught has the essential dynamical features of its atmospheric counterpart, especially in relation to that of a supercell storm, it provides an adequate basis for this study. We have therefore not attempted to 'tune' $\theta_a(z)$ and $q_a(z)$ to obtain a more realistic shape, or indeed cloud.

The maximum vertical velocity in the updraught is 20 m s^{-1} and lies within the range of values observed by Marwitz (1973) and Davies-Jones (1974). Inevitably, due to the absence of a tropopause in our model, the maximum occurs at the top of the computational domain – 8 km high – in contrast to the mean heights of 2.7 km found by Marwitz, and about 4.5 km found by Davies-Jones and Henderson (1975) in a study of 34 updraughts. Even so, Davies-

Jones and Henderson point out that the observations involve a degree of uncertainty at higher levels due to icing on the sounding balloon and sonde or on the chaff particles used by Marwitz.

The vertical distributions of temperature and dewpoint along the updraught axis and in the environment are shown in Fig. 4. Significantly, the lower part of the updraught is negatively buoyant, as is observed, but the temperature excess in the updraught is a little

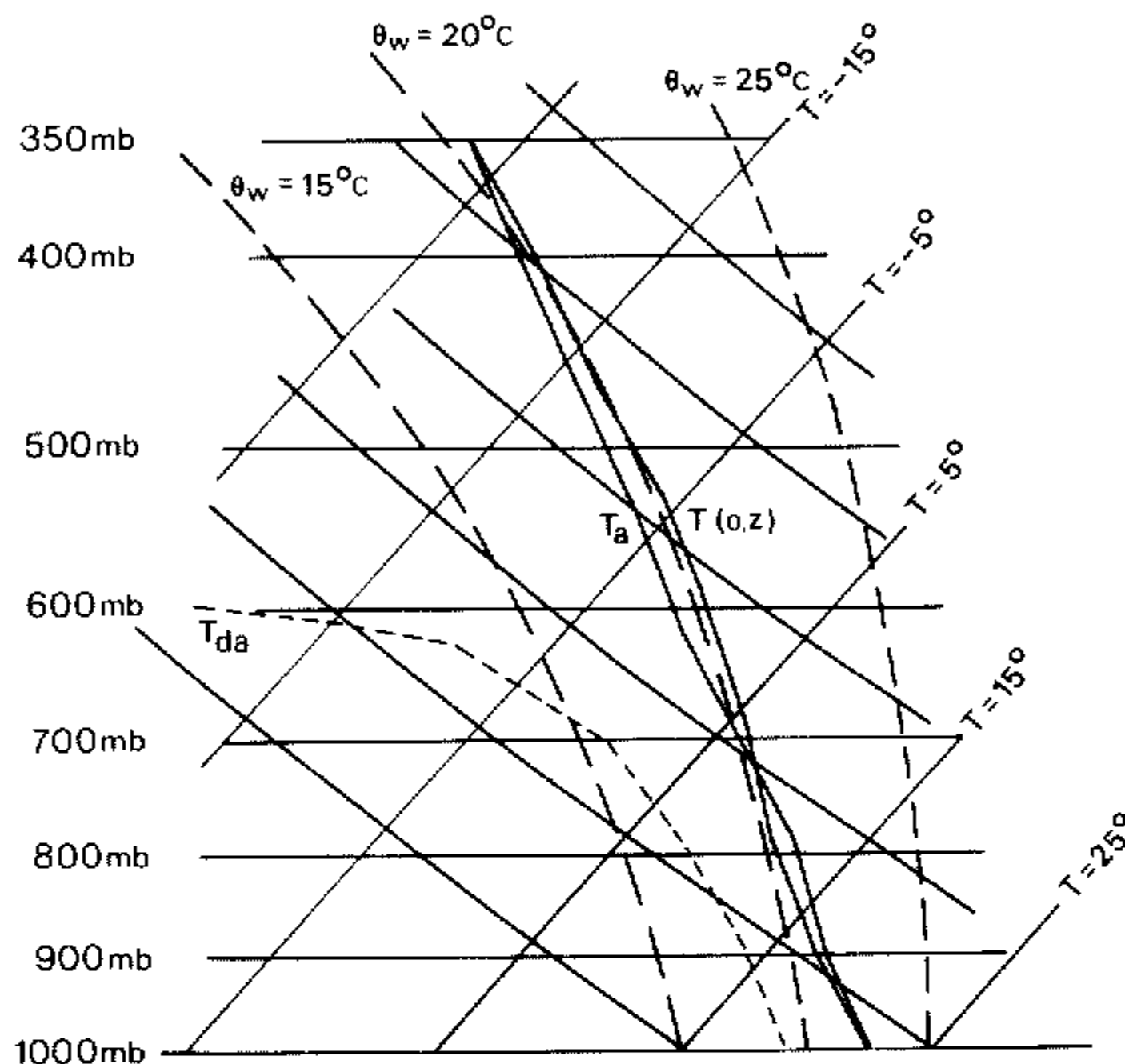


Figure 4. Vertical distributions of temperature (solid lines) along the cloud axis and in the environment in experiment 1 and the ambient distribution of dewpoint (broken line) plotted on a skew T - $\log p$ aerological diagram.

too small, being at most 2 K. Grandia and Marwitz (1975, Fig. 4b) report potential temperature differences of about 4 K in an aircraft penetration of an updraught at a height of 4.5 km, whereas Davies-Jones and Henderson (1975, Figs. 3 and 4) obtained a maximum mean virtual temperature excess of about 5 K for the 34 updraught soundings they analysed and of about 10 K for the seven fastest updraughts. We attribute the smaller excess temperatures obtained here to the relatively stable profile chosen for $\theta_a(z)$ compared with observed environmental soundings for many severe storms (e.g. the Watonga sounding reported by Davies-Jones (1974)) and it is now evident that the realistic buoyancy field, and hence the realistic updraught strength, is a result of our neglect of water loading in the cloud. However, this does not detract from the usefulness of the cloud model as a basis for the subsequent vortex calculations as the latter require only that the cloud buoyancy field be realistic. Further studies of the cloud model are in progress and will be reported in due course.

The maximum pressure reduction at the surface below the updraught is about 1 mb, which is comparable with observed values in mesolows associated with severe thunderstorms (Fujita 1963).

The subadiabatic lapse rate in the subcloud region of the updraught (Figs. 3(b) and 4) is not wholly realistic but is a consequence of the value chosen for K_H and the relatively small updraught velocities in this region; thus the radial component of diffusive heat flux is effective in raising the temperature of ascending air.

Finally, we note that outside the cloud, the streamlines and mixing ratio isopleths coincide, consistent with the conservation of moisture, whereas within the cloud there is a gradient of vapour mixing ratio along streamlines; this gradient is, of course, proportional to the local rate of condensation and hence to the rate of latent heat release.

(b) *A rotating updraught and vortex development ($V_e \neq 0$)*

Experiment 2 is identical with experiment 1 except for the imposition of the azimuthal velocity $V_e = 2.0 \text{ m s}^{-1}$ from the initial instant. In this case, air drawn in towards the axis by the growing cloud has a swirling component of motion and the updraught soon acquires a rotational structure. As development continues, a core of concentrated rotation becomes established within the cloud and subsequently extends downwards, culminating in a strong vortex at the surface. The essential stages of vortex formation in this experiment are illustrated in Fig. 5.

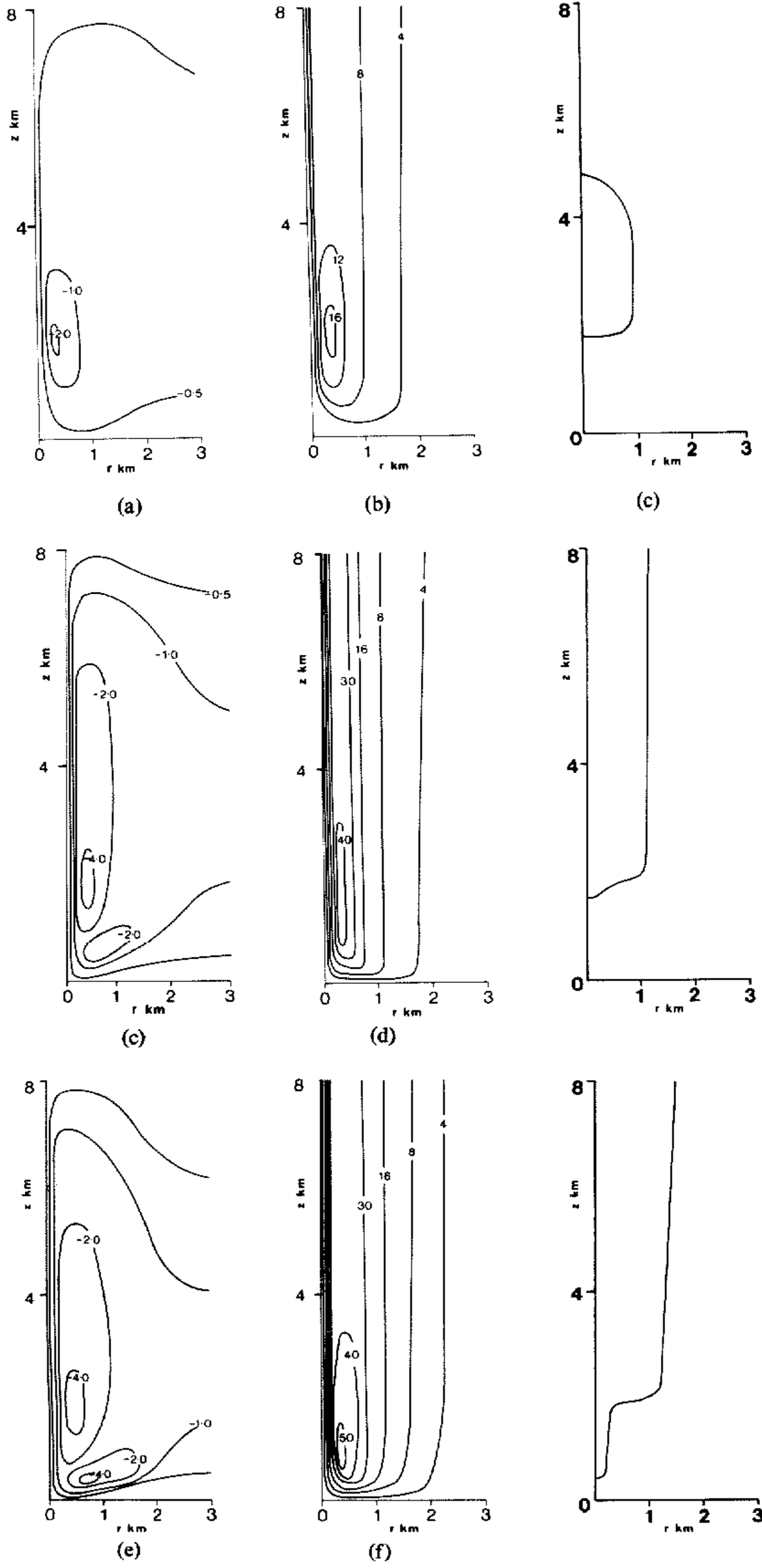
The mechanics of vortex growth are as follows. In the early stages (Figs. 5(a) and (b)) there is rapid vertical acceleration caused initially by the imposed temperature anomaly and subsequently by the release of latent heat as the temperature anomaly is 'flushed out' of the flow region. This induces radial inflow with maximum convergence in about the first kilometre above cloud base (Fig. 5(a)). As air converges, it conserves its angular momentum about the updraught and spins faster until it reaches a radius where the centrifugal force it experiences attains local cyclostrophic balance with the radial pressure force driving it: further inflow is then precluded and this rapidly rotating air is drawn upwards to form a core of concentrated rotation in the lower and middle levels of the cloud (Fig. 5(b)). This core continues to develop upwards by advection and simultaneously extends downwards in the following way. As the rotation field is established aloft, radial motion at these levels is impeded by centrifugal forces and is virtually prevented* in the vortex core. In essence, the core acts like a pipe, drawing air towards its lower end. This is evident in Fig. 5(c) where a second inflow maximum has formed near the axis below cloud base. Naturally, this inflowing air increases its rotation rate as before until cyclostrophic balance is achieved and the vortex is thereby extended (Fig. 5(d)). When the vortex reaches the ground (Fig. 5(f)), surface friction reduces the azimuthal wind speed and hence also the centrifugal forces. This prevents cyclostrophic balance and leaves a net inward pressure gradient so that a shallow but intense inflow layer is formed adjacent to the ground (Figs. 5(e) and (ei)).

The evolutionary process described above corroborates the Doppler radar observations referred to in section 1 although the vortex growth time in this experiment is about half that observed for the TVS development in the Union City tornado (Brown and Lemon 1976). Nevertheless, a more refined comparison of growth time would not be wholly meaningful because of the artificial way we have initialized our experiments and because, amongst other factors, the growth time is increased if the height of the computational region is increased (see LS) and it will presumably also increase with the radial extent of the region.

It is noteworthy that the simulated vortex extends over the full height of the computational region although the largest swirling velocities lie below 3 km, in the region near cloud base, where radial inflow is greatest and hence where rotating air achieves maximum inwards penetration (compare Figs. 5(ai) and (bi)). This is consistent with the vertical distribution of TVS intensity observed during the mature stage of the Union City tornado as shown in Fig. 6: note that the TVS intensity diminishes only slowly with height up to at least 10 km.

The maximum swirling velocity – 60 m s^{-1} in experiment 2 – corresponds with a

* Strictly, diffusive effects permit weak radial motions associated with the axial development of the core: this is shown by scaling analyses of viscous vortex cores (Morton 1969).



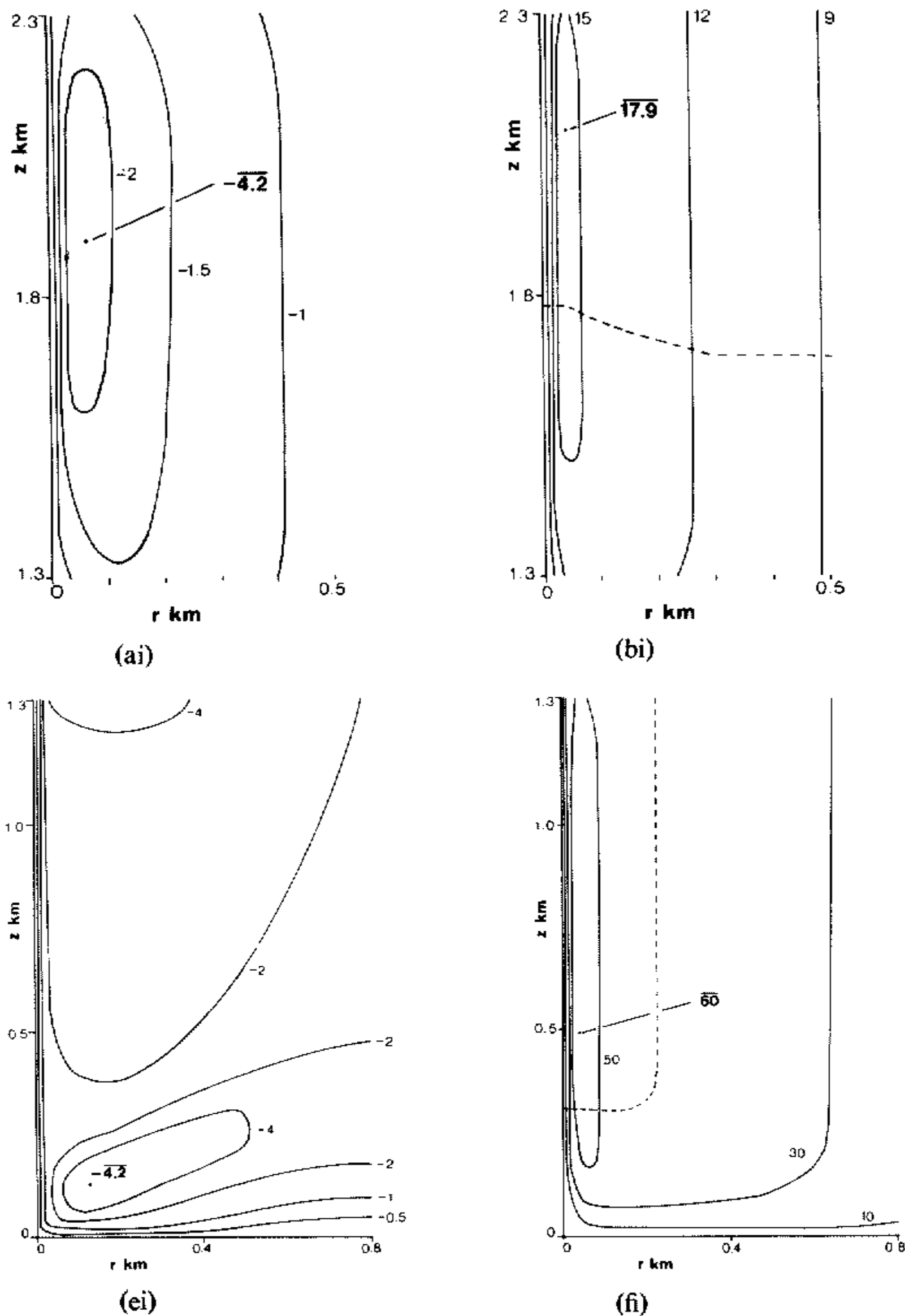


Figure 5. Stages of vortex growth in experiment 2. (a) u isotachs, and (b) v isotachs at $t = 2.5$ min; (c) u isotachs, and (d) v isotachs at $t = 9.0$ min; (e) u isotachs, and (f) v isotachs in the steady state ($t = 13.75$ min). The cloud outlines and funnel development at each of these times are shown alongside the isotach fields. In all the isotach fields the coordinates are stretched as in Fig. 3. Parts (ai) and (bi) are magnified portions of (a) and (b) respectively, drawn on a linear scale, and (ei) and (fi) are magnified portions of (e) and (f), in the regions indicated; the cloud boundary is indicated by a broken line in (bi) and (fi). Note that for the ambient temperature and moisture fields chosen, the funnel cloud is substantially broader than the vortex core. Contours are labelled in m s^{-1} ; a bar indicates the position and value of the maximum velocity component.

strong tornado and the radius of the vortex, characterized by r_{max} , is realistic. It is significant that vortex formation is accompanied by a dramatic increase in vertical velocity; here w_{max} is 63 m s^{-1} compared with 20 m s^{-1} in the non-rotating case. Vertical velocities as large as this have been inferred from photogrammetric analyses of tornado films (Hoecker 1960; Goldman 1965; Golden and Purcell 1977) and are consistent with scaling analyses of concentrated vortices (Morton 1966, 1969) which show that azimuthal and vertical velocities must have comparable orders of magnitude. It should be noted, however, that the observations rely on the presence of suitable visible tracers such as cloud tags or debris of

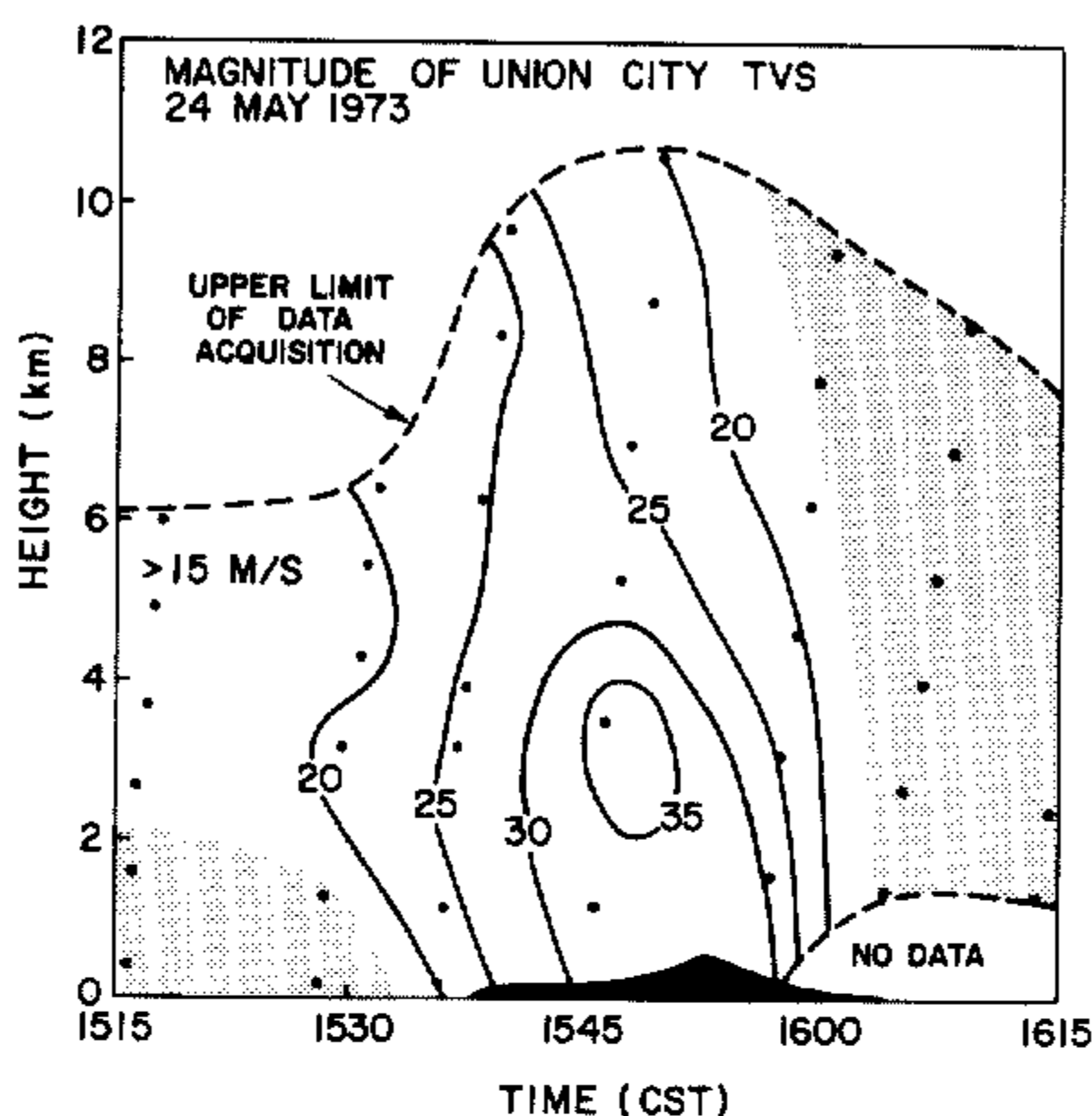


Figure 6. Time-height profile of the magnitude of the maximum Doppler velocity for each Union City TVS pair (adjusted for TVS motion). Dots indicate data points and dashed lines represent the limits of data collection. Velocity shear was less than the TVS threshold value in the lightly shaded regions. The black region at bottom centre is the diameter (using ordinate scale) of the tornado funnel near cloud base (after Brown *et al.* 1978).

various sorts and are necessarily confined to the subcloud region. There are no measurements of vertical velocities in the updraught of tornado cyclones above cloud base when a tornado is on the ground.

The reason for the large increase in vertical velocity in the presence of a vortex may be understood by further consideration of the 'pipe' analogy referred to in the context of vortex growth. Although the buoyancy field has much the same strength when $V_e = 2 \text{ m s}^{-1}$ as when there is no rotation (cf. Figs. 3(b) and 7(b) which show the isentropes in experiments 1 and 2 in the steady state), radial motion is inhibited along the length of the vortex and the meridional motion is akin to that produced by suction through a slightly porous pipe with its lower end close to a rigid boundary, and its axis normal to the boundary. Air may enter relatively freely through the end of the pipe compared with through the sides and considerable volume flux will occur in this region, resulting in large vertical accelerations (and hence velocities) at entry. For a broader and weaker vortex, equivalent to a wider pipe with larger porosity, the constraint on the meridional motion is reduced concomitant with the decrease in vertical acceleration and wind speed along the axis, in particular close to the ground. These ideas are consistent with the streamline patterns in experiments 1 and 2 (cf. Figs. 3(a) and 7(a)): note that in the vortex case, the streamlines descend towards the lower end of the vortex before ascending in the core or parallel with it. Of course, the analogy is incomplete since it ignores the motion which occurs 'outside the pipe', i.e., the motion in the immediate vortex environment which is also being driven by the buoyancy field aloft.

Further insight is provided by comparison of the vertical force field along the axis in experiments 1 and 2, as shown in Fig. 8, which includes profiles of buoyancy force $B (= g(T - T_a)/T_a)$, the vertical component of the dynamic pressure gradient $P (= -\rho^{-1}\partial p/\partial z)$ and the total vertical driving force $F (= P + B)$. In both experiments, the air is negatively buoyant at heights less than about 4 km and is driven by the dynamic pressure gradient at

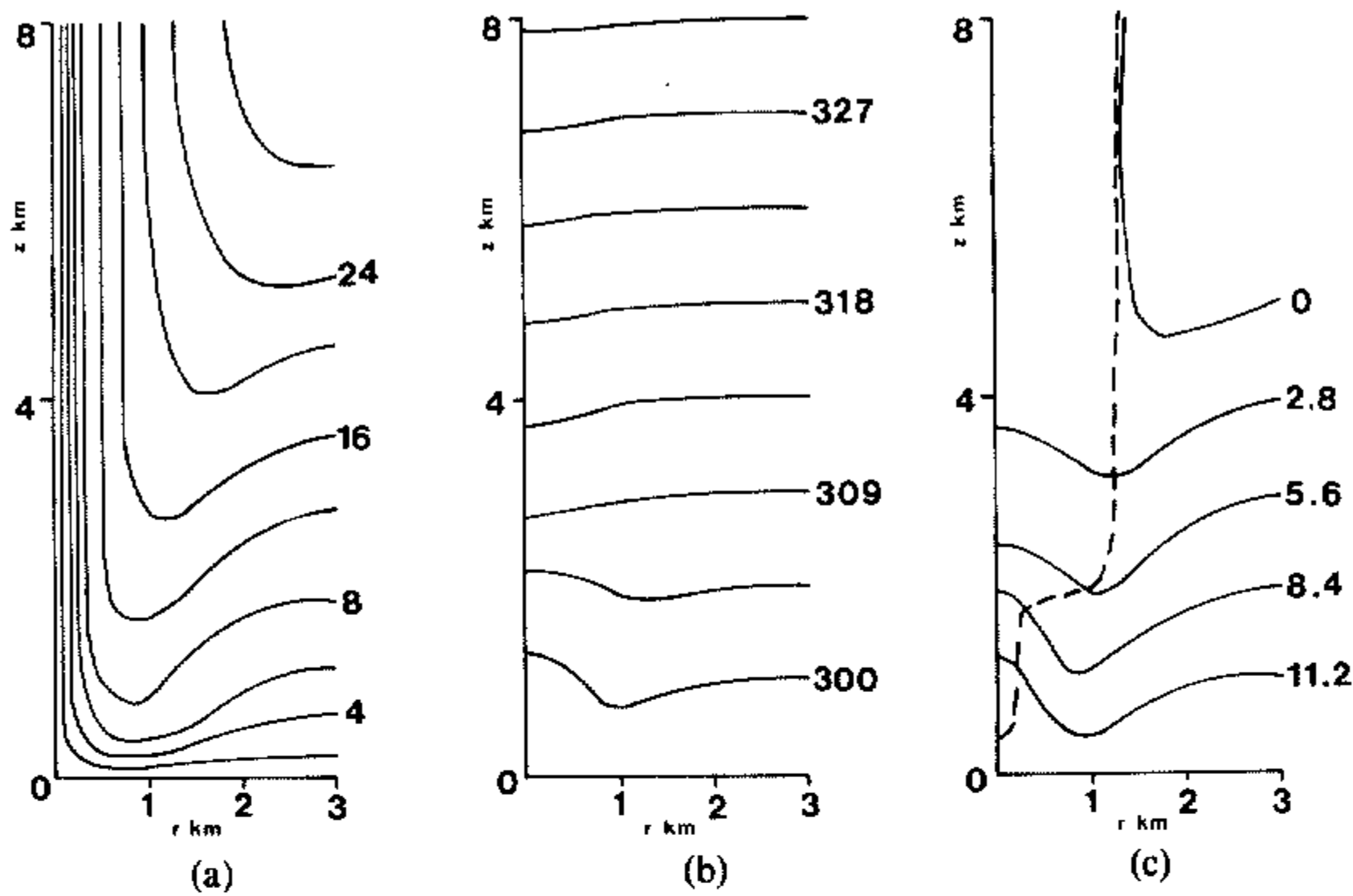


Figure 7. (a) Streamlines, with contour spacing $1.5 \times 10^6 \text{ m}^2 \text{ s}^{-1}$, (b) isentropes, labelled in K, and (c) isopleths of water vapour mixing ratio, labelled in g kg^{-1} , for experiment 2. The broken line in (c) shows the cloud outline. In (a) the coordinates are stretched as in Fig. 3.

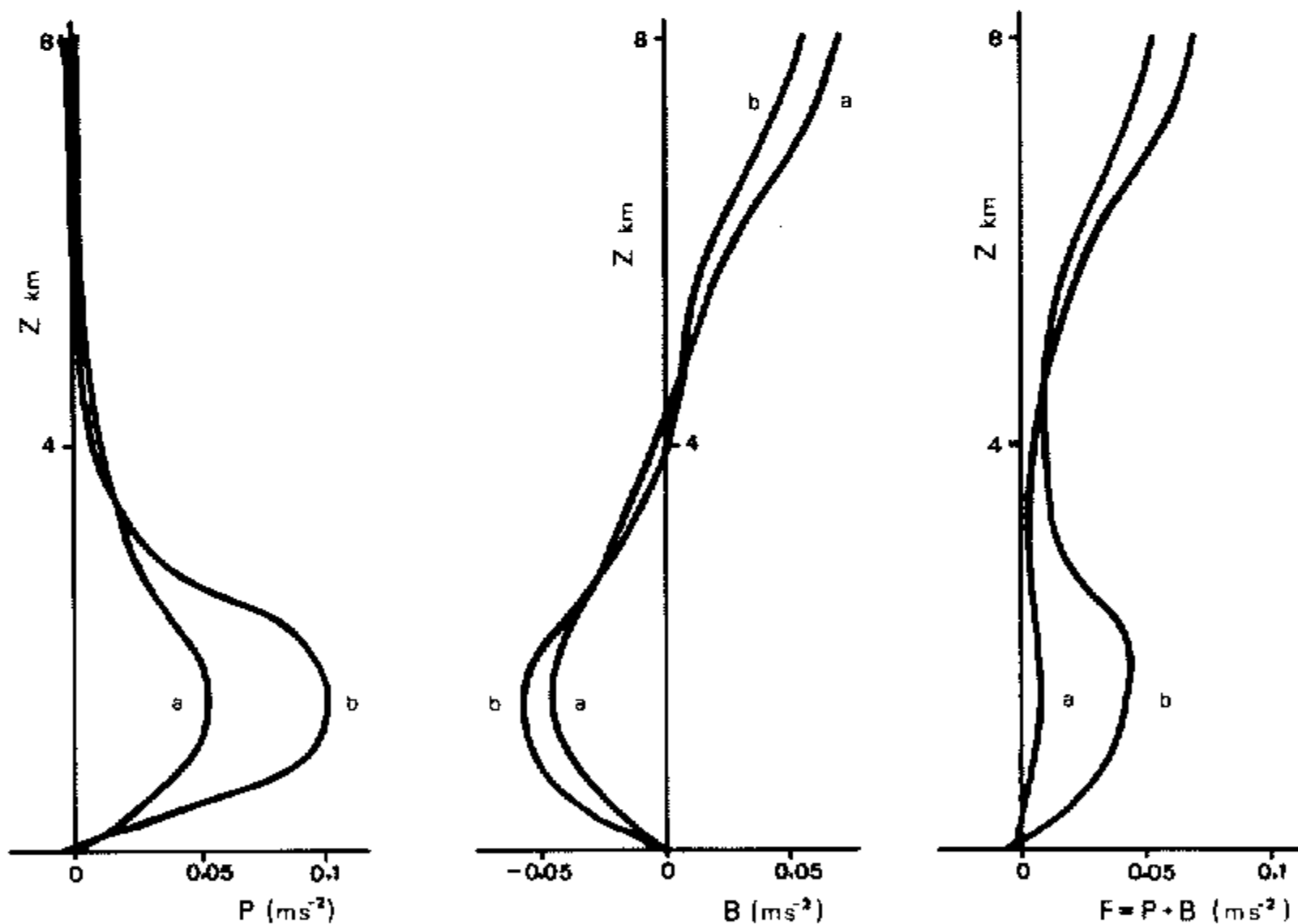


Figure 8. Profiles of vertical dynamic pressure gradient $P (= \rho^{-1} \partial p / \partial z)$, buoyancy force $B (= g(T - T_a) / T_a)$, and total vertical force $F (= P + B)$ along the axis for experiments 1 and 2 (labelled a and b, respectively, on each pair of profiles).

these levels. In experiment 2, the increased vertical motion at low levels counters the effectiveness of the radial diffusion of heat in warming the air as it ascends (see section 3(a)), but this is mostly compensated for by the latent heat release in the funnel cloud, and by the reduced air density in the vortex core due to the lower pressure there (the latter makes an important contribution to the total buoyancy force where the vortex core is strongest: see LS, Table 4). Thus the negative buoyancy is only a little larger below about 2.5 km than when rotation is absent. However, the dynamic pressure gradient is much larger and therefore the net vertical force field is considerably stronger at low levels in experiment 2, consonant with the larger vertical accelerations which occur. At upper levels, P is compara-

tively small and vertical forcing is due almost entirely to the cloud buoyancy (i.e. $F \approx B$). Above about 4.5 km, the cloud buoyancy on the axis is a little *larger* in the absence of rotation and is due to the fact that the rate of condensation with height takes place more slowly in this case. The rate of latent heat release at upper levels is therefore greater. This is evident when comparing the distributions of mixing ratio isopleths for experiments 1 and 2 as shown in Figs. 3(c) and 7(c), respectively.

(c) *Tornadoes v. funnel clouds*

In TG it is shown that concentrated vortex formation requires the driving force to lie within a narrow range of values for a given strength of imposed circulation. Moreover, the vortex extends down to the surface only if there is sufficient low level rotation (which might develop as a consequence of the meridional circulation induced by the rotating cloud) and

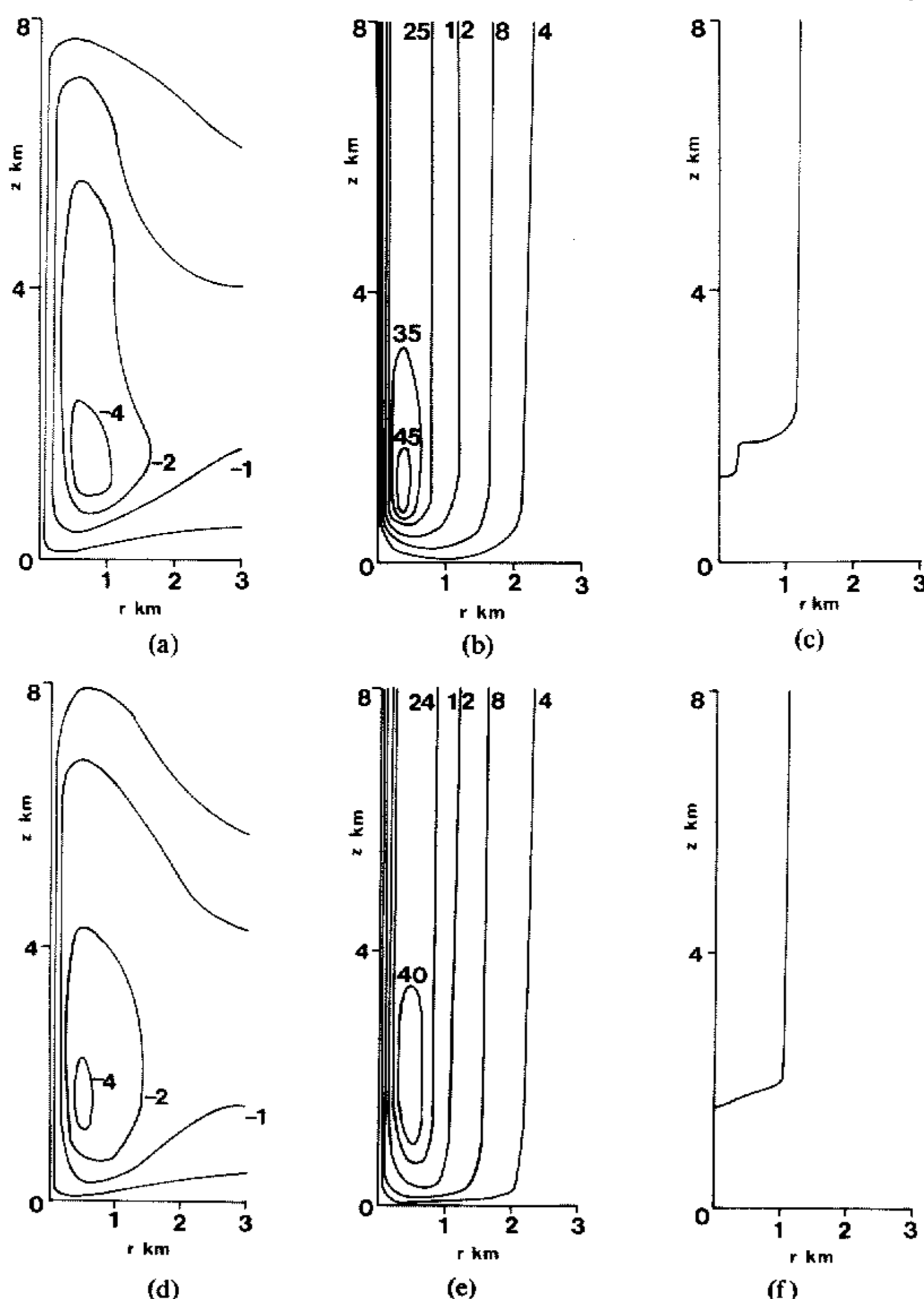


Figure 9. (a) u isotachs, (b) v isotachs, (c) cloud outline, for experiment 3 ($V_0 = 2.5 \text{ ms}^{-1}$) in the steady state; (d), (e), (f) are the corresponding fields for experiment 4 ($V_0 = 3.0 \text{ ms}^{-1}$). In the isotach fields, the coordinates are stretched as in Fig. 3, and the contours labelled in ms^{-1} .

provided the vertical stability is not too large in the lowest kilometre or so (LS): in other cases, a steady suspended vortex is formed. In this paper, we study the dependence of vortex characteristics on the level of imposed circulation, keeping all other quantities fixed, and, in experiments 3 and 4, take $V_e = 2.5 \text{ m s}^{-1}$ and 3.0 m s^{-1} , respectively. The steady-state isotachs of radial and azimuthal velocity and the corresponding cloud outlines for these experiments are shown in Fig. 9.

In experiment 3 the vortex is slightly weaker and broader than in experiment 2 (Table 2) and the pendant funnel cloud terminates above 1.2 km (Fig. 9(c)). High swirling velocities occur below this level (Fig. 9(b)) but the absence of a pronounced inflow maximum near the surface (Fig. 9(a)) indicates only weak frictional interaction with the lower boundary compared with experiment 2. These trends are even more pronounced in experiment 4 where the vortex is not only weaker and broader, but clearly terminates aloft with the funnel cloud barely discernible. These results are as expected. Clearly, an increase in the imposed circulation, keeping other parameters fixed, increases the rotational forces opposing inflow so that cyclostrophic balance is achieved at larger radii. This leads to a broader vortex with weaker upflow and, as the calculations show, to smaller swirling velocities. Ultimately, as the imposed circulation is increased further, one would anticipate the occurrence of downflow on part of the vortex axis as, for example, in the case of dust devils (Smith and Leslie 1976), but by this stage the vortex would be quite weak for the cloud parameters we have chosen. A photogrammetric analysis of the small but rather stable 1957 Dallas tornado by Hoecker (1960) provides some evidence for the existence of downflow in the tornado, but whether this is characteristic of all, or many, tornadoes remains an open

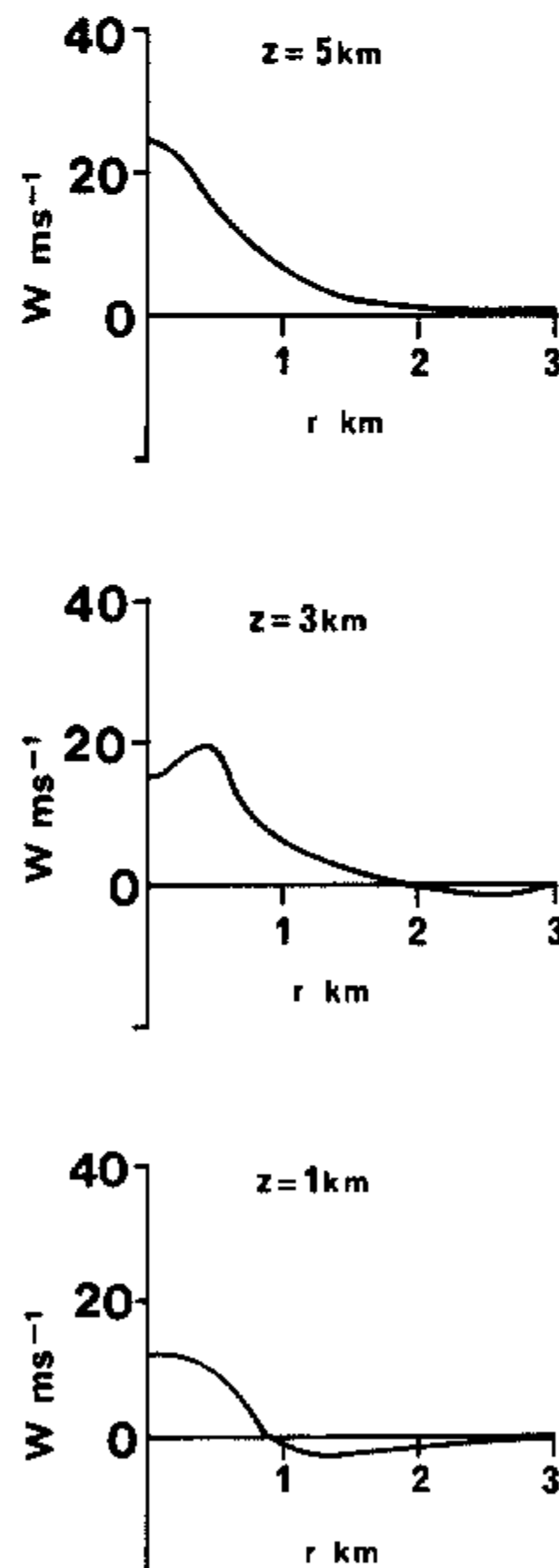


Figure 10. Radial profiles of vertical velocity at heights of 1, 3 and 5 km in experiment 4.

question (see Morton 1966, pp. 155–156). It is known, of course, that an adverse axial pressure gradient is induced in regions where a vortex decays and/or broadens with height (Morton 1969, pp. 318–319) and may lead to axial downflow if it is strong enough to negate any buoyancy force. However, in these experiments, this effect is only strong enough to cause reduced upflow near the axis and it is pronounced only in experiment 4.

This is illustrated in Fig. 10 which shows the radial profile of vertical velocity at heights of 1, 3 and 5 km: note that at 3 km, where the vortex decays rapidly with height (Fig. 9(e)), the maximum vertical velocity is displaced a slight distance away from the axis.

The dependence of vortex parameters r_{\max} , v_{\max} and w_{\max} on the magnitude of the imposed swirling velocity V_e is shown in Fig. 11, which is constructed using Table 2 and the results of two further experiments (not listed in Table 1), similar to experiment 2 but with $V_e = 0.5$ and 1.0 m s^{-1} . The sharpness of the peaks in the curves $v_{\max}(V_e)$ and $w_{\max}(V_e)$ indicates, for fixed ambient distributions of temperature and moisture, the degree to which

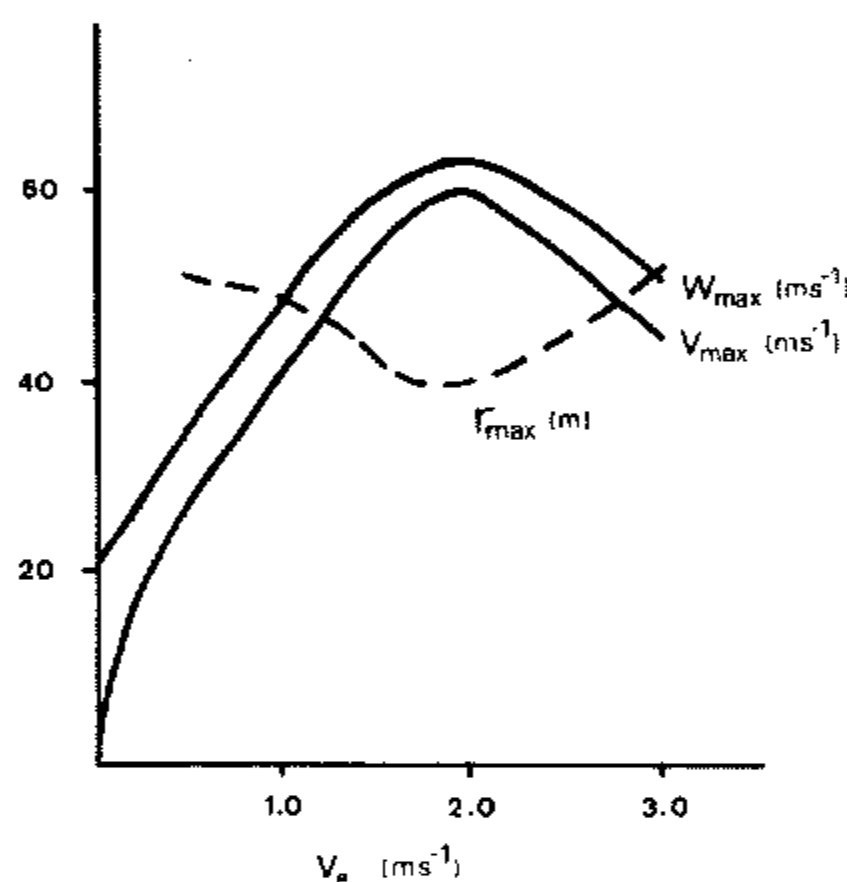


Figure 11. Variations of r_{\max} , v_{\max} and w_{\max} as functions of V_e .

the circulation must be ‘tuned’ to produce a concentrated vortex. Note that, for the temperature and moisture distributions used here, the narrowest and most intense vortex occurs when V_e is only slightly smaller than 2 m s^{-1} , almost coincident with experiment 2. As V_e declines from this value, both v_{\max} and w_{\max} decrease but r_{\max} increases. There is a temptation to argue that the reduced rotational constraint should allow rotating air to be drawn into a smaller radius before cyclostrophic balance is attained, thereby reducing r_{\max} , but this ignores the effect of the reduced constraint on the shape of the meridional streamlines. Thus air which enters through the radial boundary at a given height follows a steeper trajectory as V_e declines, so that the minimum radius it attains is increased. These two factors are in opposition for $V_e \lesssim 2 \text{ m s}^{-1}$ but otherwise reinforce each other so that the arguments given earlier for the behaviour of r_{\max} , etc. as V_e increases above 2 m s^{-1} , remain valid. It should be noted that the variations shown in Fig. 11 are similar to those in Fig. 5 in TG, but in the latter, the vortex driving force is varied, keeping the imposed circulation fixed.

(d) Surface friction effects

In the absence of any detailed estimates of diffusivity distributions in tornadoes, we have deliberately resisted the use of variable coefficients K_M and K_H in our models. However, we recognize the crudeness of the assumption of constant K_M , especially in the terminating friction layer when it is taken in conjunction with the no-slip condition at the surface. Since

this layer is believed to play an important role in vortex dynamics, principally through the strong dynamic coupling it exerts between the azimuthal and meridional components of the vortex circulation, we have studied the effects of alternatives to the no-slip condition at the surface.

Perhaps a more appropriate formulation near the ground is to assume aerodynamically rough flow in a relatively thin sublayer adjacent to the surface, and across which the shear stress is uniform and K_M is proportional to z (Priestley 1959, Ch. 3). To a first approximation, it would appear reasonable to ignore the mass flux in this sublayer and parameterize its effect by the surface boundary condition $(\partial u/\partial z, \partial v/\partial z) = C_D(u^2 + v^2)^{1/2}(u, v)$ at $z = 0$, where C_D is a constant with dimensions $m^{-2}s^{-1}$, determined by the details of the sublayer. Accordingly, we were led to carry out experiments 5 and 6 in which the no-slip condition in experiment 2 is relaxed to partial slip, with $C_D = 1 m^{-2}s^{-1}$, and free slip, with $C_D = 0 m^{-2}s^{-1}$, respectively (the former value is chosen arbitrarily to provide an intermediate

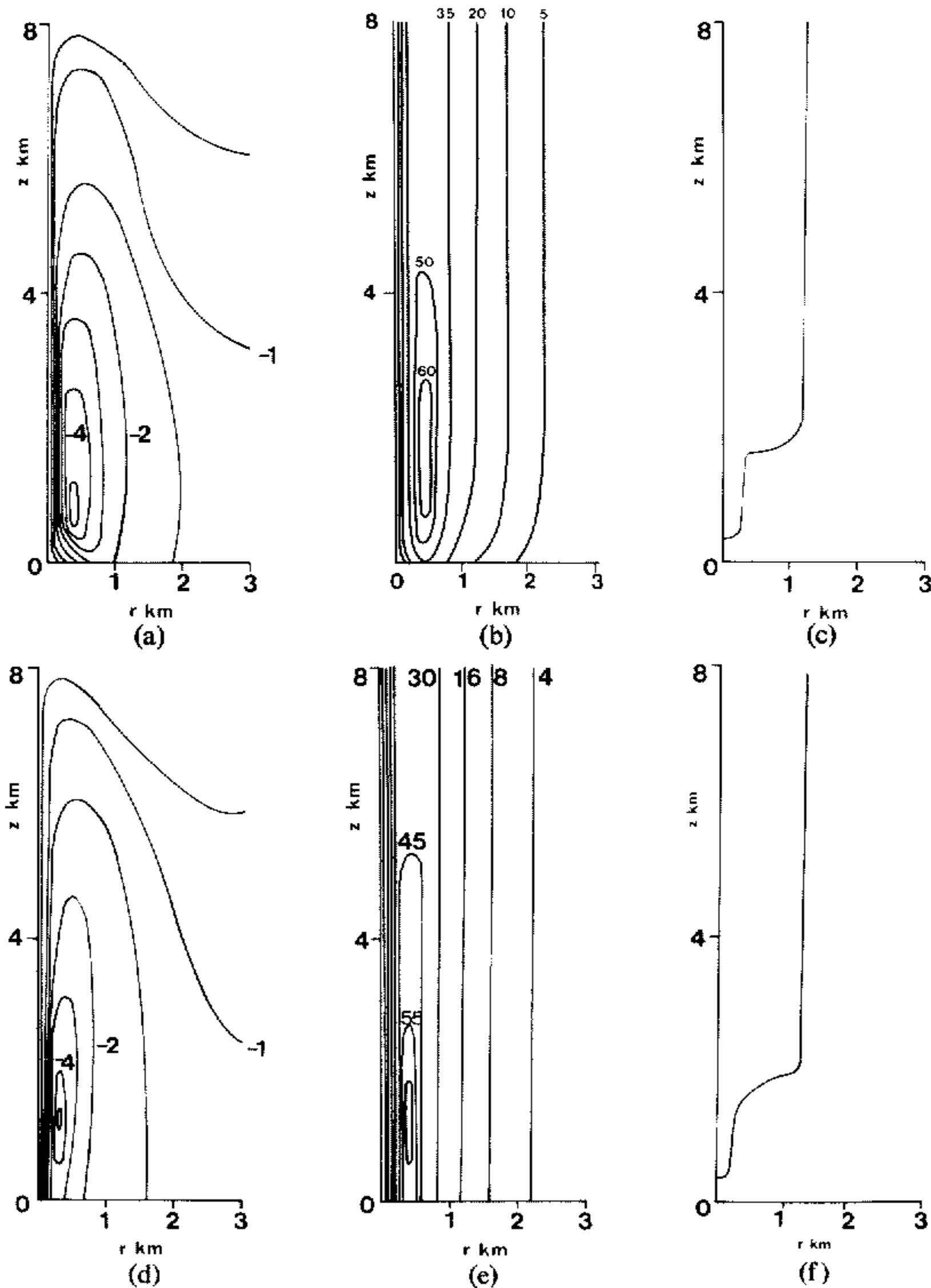


Figure 12. (a) u isotachs, (b) v isotachs, (c) cloud outline, for experiment 5 ($C_D = 1.0 m^{-2}s^{-1}$) in the steady state; (d), (e), (f) are the corresponding fields for experiment 6 ($C_D = 0 m^{-2}s^{-1}$). Legend otherwise as in Fig. 9.

case between the extremes of no slip and free slip). The steady-state isotachs of radial and swirling velocity and the cloud outlines for these two experiments are shown in Fig. 12, and other data (r_{\max} , v_{\max} , etc.) are included in Table 2. In both cases, strong vortices form and their funnel clouds terminate within about 300 m of the surface. In general, as the surface frictional constraint declines, radial motion is less restrained and air trajectories shift slightly inwards. For this reason, and because the boundary torque is also reduced, the swirling velocities increase (note that v_{\max} is about 17% larger in experiment 6 than in experiment 2). The distribution of inflow is also altered; inflow becomes significant over a substantial vertical depth and the second inflow maximum close to the boundary in experiment 2 disappears. However, the maximum inflow occurs below cloud base. Evidently, the absence of a secondary inflow maximum at low levels is sufficient to cause a marginal reduction in vertical velocity (in experiment 6, w_{\max} is about 6.5% less than in experiment 2) but does not significantly restrict the supply of low-level moisture to the vortical updraught.* For this reason, the terminating inflow layer appears to have a less important control on the vortex dynamics than has previously been supposed. These results are similar to those obtained by Bode *et al.* (1975) for vortices in a homogeneous fluid driven by an axial body force, the difference here being that the buoyancy driving force is itself a function of the frictionally induced convergence at the lower boundary.

ACKNOWLEDGMENTS

We wish to record our thanks to Bob Davies-Jones of NSSL for his very valuable comments on an earlier version of the manuscript and to Doug. Lilly of NCAR with whom one of us (RKS) had a stimulating discussion about the work. We also thank Rodger Brown of NSSL for providing us with Fig. 6.

REFERENCES

- | | | |
|---|-------|---|
| Bode, L., Leslie, L. M. and Smith, R. K. | 1975 | A numerical study of boundary effects on concentrated vortices with application to tornadoes and waterspouts, <i>Quart. J. R. Met. Soc.</i> , 101 , 313–324. |
| Brandes, E. A. | 1977a | Flow in severe thunderstorms observed by dual-Doppler radar, <i>Mon. Weath. Rev.</i> , 105 , 113–120. |
| | 1977b | Mesocyclone evolution and tornado generation within the Harrah, Oklahoma storm, <i>NOAA Tech. Memo. ERL NSSL-81</i> . |
| Brown, R. A. and Lemon, L. R. | 1976 | Single Doppler radar vortex recognition: part II – tornadic vortex signatures, <i>Proc. 17th AMS Conf. on Radar Met.</i> , Seattle, 104–109. |
| Brown, R. A., Lemon, L. R. and Burgess, D. W. | 1978 | Tornado detection by pulsed Doppler radar, <i>Mon. Weath. Rev.</i> , 106 , 29–38. |
| Browning, K. A. | 1965 | The evolution of tornadic storms, <i>J. Atmos. Sci.</i> , 22 , 664–668. |
| Browning, K. A. and Foote, G. B. | 1976 | Airflow and hail growth in supercell storms and some implications for hail suppression, <i>Quart. J. R. Met. Soc.</i> , 102 , 499–533. |
| Burgess, D. W. | 1976 | Single Doppler radar vortex recognition: part I – mesocyclone signatures, <i>Proc. 17th AMS Conf. on Radar Met.</i> , Seattle, 97–103. |
| Burgess, D. W., Lemon, L. R. and Brown, R. A. | 1975a | Tornado characteristics revealed by Doppler radar, <i>Geoph. Res. Letters</i> , 2 , 183–184. |
| | 1975b | Evolution of a tornado signature and parent circulation as revealed by single Doppler radar, <i>16th Radar Meteorology Conference</i> , Houston, Texas (American Meteor. Soc.), 99–105. |

* This is in contrast to the situation in a tropical cyclone, where the convergence of moisture in the boundary layer is crucial to the dynamics of the vortex. However, the aspect ratio is also quite different, the breadth of a tropical cyclone being comparatively large compared with its depth.

- Danielsen, E. F. 1975 A conceptual theory of tornadogenesis based on macro-, meso- and microscale processes, *Proc. 9th AMS Conference on Severe Local Storms*, Norman, 376–383.
- Davies-Jones, R. P. 1974 Discussion of measurements of high-speed thunderstorm updrafts, *J. Appl. Met.*, **13**, 710–717.
- Davies-Jones, R. P. and Golden, J. H. 1975 On the relation of electrical activity to tornadoes, *J. Geoph. Res.*, **80**, 1614–1616.
- Davies-Jones, R. P. and Henderson, J. H. 1975 Updraught properties deduced statistically from rawin soundings, *Pure and Appl. Geoph.*, **113**, 787–801.
- Davies-Jones, R. P. and Kessler, E. 1974 Tornadoes, article in *Weather and climate modification*, Ed. W. N. Hess, John Wiley, 552–595.
- Eskridge, R. E. and Das, P. 1976 Effect of a precipitation-driven downdraft on a rotating wind field: a possible trigger mechanism for tornadoes? *J. Atmos. Sci.*, **33**, 70–84.
- Fujita, T. 1963 Analytical mesometeorology. A review, *Met. Mon.*, **5**, No. 27, 77–125.
- Golden, J. H. and Purcell, D. 1977 Photogrammetric velocities for the Great Bend, Kansas, tornado of 30 August 1974: accelerations and asymmetries, *Mon. Weath. Rev.*, **105**, 485–492.
- Goldman, J. L. 1965 The Illinois tornadoes of 17 and 22 April 1963, *SMRP Res. Paper No. 39*, Univ. of Chicago, Dept. of Geophysical Sciences.
- Grandia, K. L. and Marwitz, J. D. 1975 Observational investigations of entrainment within the weak echo region, *Mon. Weath. Rev.*, **103**, 227–234.
- Hess, S. L. 1959 *Introduction to theoretical meteorology*, Holt, Rinehart and Winston, New York.
- Hoecker, W. H. 1960 Wind speed and airflow patterns in the Dallas tornado of 2 April 1957, *Mon. Weath. Rev.*, **88**, 167–180.
- Leslie, L. M. and Smith, R. K. LS 1978 The effect of vertical stability on tornadogenesis, *J. Atmos. Sci.*, **35**, 1281–1288.
- Marwitz, J. D. 1972 The structure and motion of severe hailstorms. Part I: Supercell storms, *J. Appl. Met.*, **11**, 166–179.
- 1973 Trajectories within the weak echo regions of hailstorms, *Ibid.*, **12**, 1174–1182.
- Morton, B. R. 1966 Geophysical vortices, *Prog. in Aeronautical Sci.*, **7**, 145–194 (ed. D. Küchemann), Pergamon.
- 1969 The strength of vortex and swirling core flows, *J. Fluid Mech.*, **38**, 315–333.
- Ogura, Y. and Phillips, N. A. 1962 Scale analysis of deep and shallow convection in the atmosphere, *J. Atmos. Sci.*, **19**, 173–179.
- Priestley, C. H. B. 1959 *Turbulent transfer in the lower atmosphere*, University of Chicago Press.
- Rossmann, F. O. 1960 On the physics of tornadoes, in *Cumulus dynamics*, Ed. Anderson, Pergamon.
- Smith, R. K. and Leslie, L. M. 1976 Thermally driven vortices: a numerical study with application to dust-devil dynamics, *Quart. J. R. Met. Soc.*, **102**, 791–804.
- TG 1978 Tornadogenesis, *Ibid.*, **104**, 189–199.
- Smith, R. K., Morton, B. R. and Leslie, L. M. 1975 The role of dynamic pressure in generating fire wind, *J. Fluid Mech.*, **68**, 1–19.
- Smith, R. K., Mansbridge, J. V. and Leslie, L. M. 1977 Comments on 'Effect of a precipitation-driven downdraft on a rotating wind field: a possible trigger mechanism for tornadoes?' *J. Atmos. Sci.*, **34**, 548–549.
- Wilhelmson, R. and Ogura, Y. 1972 The pressure perturbation and the numerical modelling of a cloud, *Ibid.*, **29**, 1295–1307.
- Williams, G. P. 1969 Numerical integration of the three-dimensional Navier-Stokes equations for incompressible flow, *J. Fluid Mech.*, **37**, 727–750.